Guiding severely anisotropic twinning bands in Magnesium: An in situ investigation by full-field microscopic image correlation

Sefer Can Erman, Laurent Stainier, Cahit Can Aydıner

Guiding severely anisotropic twinning bands in Magnesium: an in situ investigation by full-field microscopic image correlation

S. Can Erman[1], Laurent Stainier[2], C. Can Aydıner[1,*]

[1]Department of Mechanical Engineering, Boğaziçi University, Bebek, Istanbul, 34342, Turkey

[2]Nantes Université, Ecole Centrale Nantes, CNRS, GeM (UMR 6183), F-44000 Nantes, France

ABSTRACT

A critical issue for lightweight Magnesium alloys is their propensity for strain localization at the component scale, linked to the peculiar twinning phenomenon. For the (c-axes-aligned) rolling texture, highly compact coordinated twinning bands (CTBs) form that, uniquely, have a singular plane of shear. Normally, where these bands emerge, and progress are up to stochastic factors. Here, a cross-notched sample design is nominated to guide the bands of conjugate orientations into predetermined diagonal corridors and enforce their overlap at a prefixed location. The deformation fields in the Magnesium AZ31 sample are in situ monitored with an advanced microscopic image correlation (micro-DIC) variant that has a unique combination of extreme field coverage (~1.5×10^5 grains), intragranular resolution (~10^2 data points per grain) and very high time-step resolution (0.05-0.1% nominal strain increments over the twin plateau). The latter allows investigating the emergence, advance, lateral growth, and interaction of CTBs with extreme detail over absolute and sequential micro-DIC strain maps. The sample design is successful in guiding the CTB formations into the designated corridors. Seed segments of CTBs first make a cross connection across the sample, followed by lateral expansion that proceeds until the corridor is roughly filled. This happens sequentially for the two diagonal corridors, forcing the second band to pass through the first. The band strain is reduced by about 25% at the enforced overlap compared to the characteristic intensity it exhibits outside it (around 2.3%)—a direct measurement of the dilution of the strain activity of a CTB as it crosses another CTB. The uniqueness of this application in guiding severely anisotropic bands is contrasted with the micro-DIC fields of a transversely isotropic sample of the same material that is analogously put under a twin-dominated deformation.

Keywords: magnesium, twinning, coordinated twinning bands, digital image correlation, microscopy

INTRODUCTION

Desirable as the lightest structural metals, hexagonal close packed Magnesium and its alloys are riddled with the complexity of their mechanical behavior. They possess a variety of slip (basal, prism, pyramidal) and mechanical twin systems [1] that are activated to different degrees depending on orientation distribution and load path [2–4]. Further, twin operation is unidirectional. The most commonly observed twin system, $\{10\bar{1}2\}(\bar{1}011)$ tensile twin, shows profuse activity only when the load sense favors its operation [5,6]. Consequently, the behavior of these materials is severely load-path dependent [7], typified by the asymmetry of their cyclic (tension-compression) stress-strain curves [8–10]. The inherent complexity of strain accommodation in Magnesium alloys demands fundamental-scale approaches in forming universal models of these materials. In particular, immense effort has been put on crystal plasticity implementations [11–14] in the recent years. The sophistication of these models

*Corresponding author. E-mail: can.aydiner@boun.edu.tr

has advanced steadily, and, currently, high fidelity is pursued even for local (crystallite-scale) fields of stress, strain, and twin volume fraction [14–18].

A deep challenge for these models that again stems from the tensile twin mechanism is long-range strain localization across the polycrystal [19–25]. Crudely, abrupt twin emergence in one grain triggers a twin in its neighbor, successively forming a chain effect that culminates in macroscopic strain bands. While these bands and their microstructural dependencies have been studied [26,27], multi-face, multi-scale digital image correlation (DIC) measurements have only recently detailed the kinematics of these bands [22–24]. In the most common rolled material with the sharp, c-axes-aligned crystallographic texture, the anisotropy of the coordinated twinning bands (CTBs) is found to be at the material limit, largely akin to a single crystal that deforms with only two slip systems that operate ±45° to the load [22]. As shown in Figure 1, the measurement of effective strain ratios (apparent Poisson's ratio, ν) of these deformation bands yields virtually 1 over the RD-ND plane and 0 over the orthogonal RD-TD plane under RD compression (RD/TD/ND are rolling/transverse and normal directions of the plate). 1 and 0 are indeed limiting values for ν measured on orthogonal planes for an isochoric deformation structure, to be compared to 0.5 on both planes in the case of isotropic plasticity [23,24,28].

A critical issue with deformation via autocatalytic twin proliferation is the unpredictability of the position of the CTBs. The location of the emergence and procession of the abrupt band attacks are up to random factors like microstructural variations. It is clearly desirable and technologically important to regularize the activity of these bands, i.e., control the position of these deformation structures and their encounters.

In the current study, we present a sample design that preordains the location of the shear bands and, in particular, ensures the overlap of the shear bands at an exact region. We monitor the fields in situ with an in-house microscopic DIC instrument that combines grain-scale resolution with macroscopic coverage by large-field area-scanning. This instrument is uniquely able to utilize high-resolution (high numerical aperture, low depth of field) objectives with automated correction measures. While this maximizes the spatial resolution over a gross field of approximately 1.5×10^5 grains, this effort further features an extraordinary time-step resolution to in situ elucidate the emergence, advance, and interaction of the bands over fine load increments.

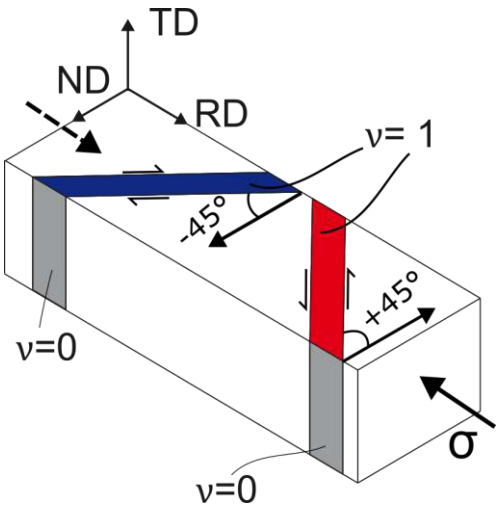

Figure 1. Geometric description of the extremely anisotropic twinning bands in rolled Magnesium polycrystals. RD/ND/TD stand for rolling/normal/transverse directions. The plane of shear of the bands is strictly the RD-ND plane. The strain ratio (apparent Poisson's ratio), ν, measured over the band zones is indicated over RD-ND and TD-RD sections.

MATERIALS AND METHODS

In view of the strict orientation that the coordinated twinning bands exhibit (Fig. 1), a notched sample design that attempts to guide and confine their activity is derived. Firstly, for the imposed RD-compression, the notches should be carved strictly along the TD direction. Secondly, the notches to guide a single band should be vertically offset on two sides of the sample, contrary to the typical notched sample geometry that is symmetric about the load axis. If a nominal +45° (-45°) band is targeted, the notch on the right side of the sample is to be accordingly higher (lower). As detailed in Fig. 2, the current sample design contains two sets of offset-notch pairs: (i) bottom left (BL) and top right (TR) to incite a nominal +45° band and (ii) top left (TL) and bottom right (BR) to incite a nominal -45° band. The idea in guiding both families of shear bands is to enforce their overlap. In regular samples, where the location and advance of the bands is unpredictable, it is possible that one family shows dominant activity over the other (e.g., [23]). Further, even when both band families are activated, their initial tendency is to avoid each other similar to the depiction in Fig. 1 [24,29]. The enforced overlap in this sample design allows us to single out and study the deformation physics of the band interaction. The relative alignment of the BL-TR and TL-BR notch pairs predetermines the position of the enforced band overlap. In this design, these pairs are placed symmetrically to position the overlap at the sample center, apparent as the diamond shaped domain in Fig. 2.

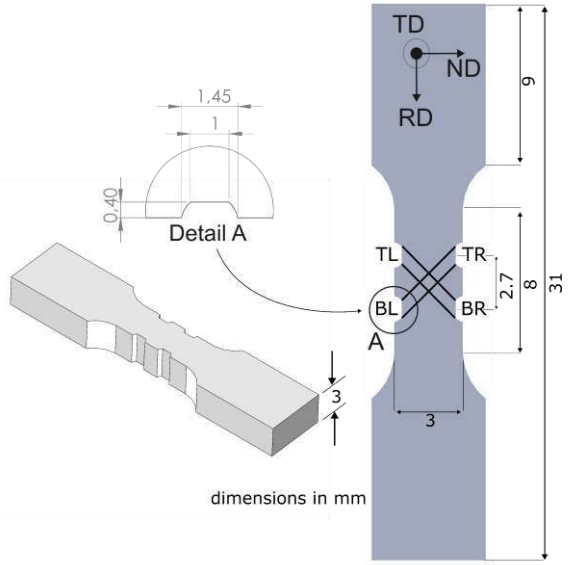

Figure 2. Detailed geometry of the notched sample design. Notches are denoted BL, TL, BR, TR (BL=bottom left, TR=top right, etc.). The coordinated twinning bands that are intended to be guided by BL-TR and TL-BR notch pairs are indicated with solid lines on the top view of the sample.

The designed geometry is extracted by wire electric discharge machining (EDM) from a 6.35 mm thick Mg AZ31B hot rolled plate procured from Alfa Aesar with the load axis aligned with the RD. The nominal thickness of the sample matches its nominal width (3 mm) to preclude buckling about either axis. The sample surface is grinded (grit sizes P1200 down to P4000), polished (colloidal silica, 0.06 µm particle size) and etched (picric acid solution [28]) to remove the EDM layer, achieve microscopic flatness, and reveal grain boundaries. Subsequently, the DICpattern is introduced by spraying a paint-ethanol mixture using an Iwata Custom Micron CM-B airbrush.

Figure 3(a) shows a sketch of the experimental setup (further details in [29]). The loading fixture (a Kammrath&Weiss, 10 kN tension-compression module) is positioned on top of Newport X/Y/Z positioning stages. The vertical macro- and micro-DIC optical lines are stationary. The micro-DIC line consists of a FLIR Grasshopper 3 camera with a 5 MP Sony IMX250 monochrome sensor and a Navitar Ultrazoom 6000 tube lens assembly with a high-resolution, long working distance Mitutoyo M Plan

APO 20x objective at its tip with 0.42 numerical aperture (NA), 20 mm working distance (WD), and 1.6 µm depth of field (DOF). (The very limited depth of field implies immediate defocusing under deformation without corrective measures.) The nominal total magnification of the micro-DIC line is 40x. Due to the miniature size of the sample, the optics on the macro-DIC line is still a low-powered microscope (an Edmund Optics zoom inspection microscope head at 1x). The optical resolution of the micro and macro-DIC lines are 0.1 and 5.67 µm/pixel, respectively. The setup is vibrationally isolated over a Newport RS4000 optical table.

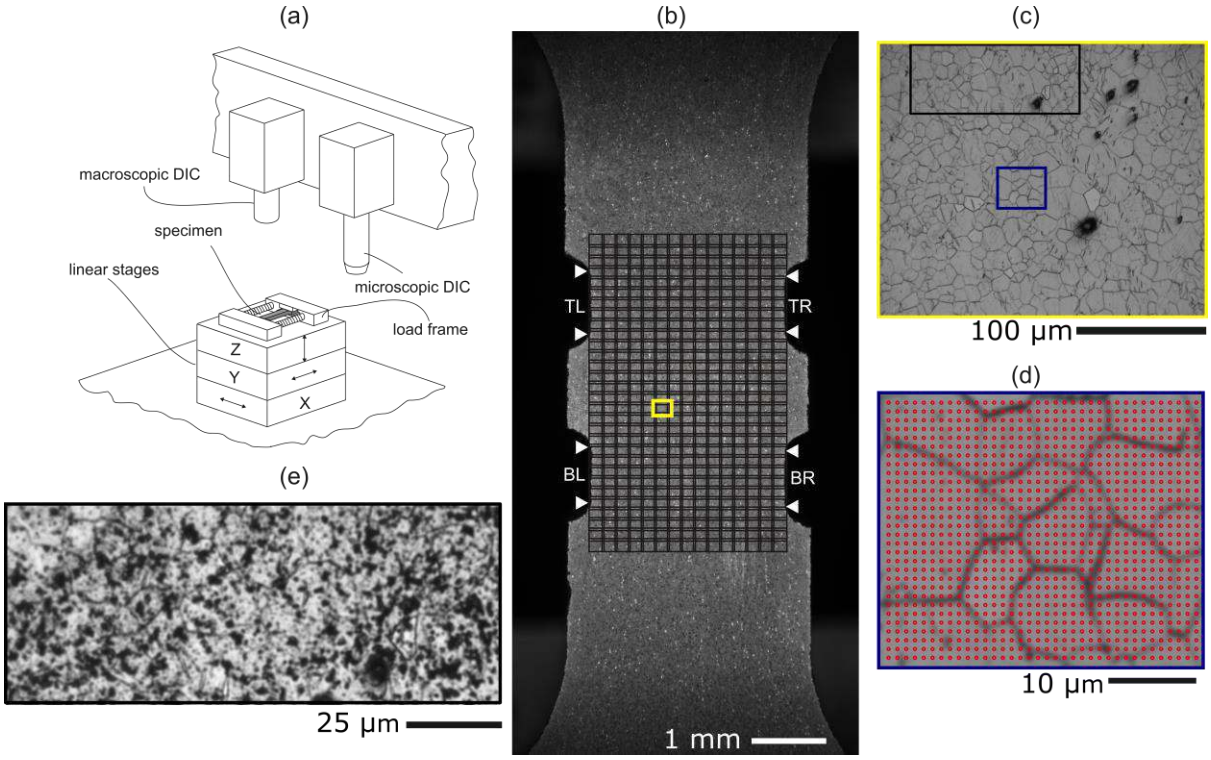

Figure 3. (a) Sketch of the setup, (b) a sample macro-DIC image of the sample over which the micro-DIC scan of overlapping 450 micrographs is shown, (c) a single micrograph (yellow box in (b)) from the scanned field, (d) a smaller granular neighborhood (blue box in (c)) with the utilized DIC grid overlaid with red dots. The images (c,d) are recorded after metallography but before patterning. (e) The image of a grain field (black box in (c)) after the DIC paint pattern is introduced.

The sample is compressively loaded in position control with fine strain increments (on average 0.026%, 84 macro-DIC data points) up to a -2.2% average strain. At each load increment, the macro-DIC images are recorded (see Fig. 3(b) for a sample image) and analyzed in real time to check the progress of strain fields. At selected loads, the sample is sent under the micro-DIC line for a 30×15 area scan of overlapping microscopic images. This array of frames is shown over the macro-DIC photo in Fig. 3(b). The resolution of the resulting ~1.5 Gigapixel combined micro-DIC image (covering 3.10×4.97 mm^2) cannot be represented by a full-field plot on paper, and hence, a single frame (highlighted in Fig. 3(b)) is shown in Fig. 3(c), covering 244×204 μm^2. For clear presentation of the grain morphology, the image of Fig. 3(c) is taken from a pre-experiment scan that is recorded after metallography but before patterning. A further zoom into a small grain neighborhood (blue box, Fig. 3(c)) is shown in Fig. 3(d). Fig. 3(e) exemplifies the image intensity fields after speckle addition over a 130×54 μm^2 region (black box, Fig. 3(c)) that contains about 90 grains. The combined micro-DIC field [Fig. 3(b)] encompasses approximately 1.5×10^5 grains and the average grain size is determined by the lineal intercept method as 10.1 µm.

The strain interval of the micro-DIC scans range between 0.05-0.1% (30 points up to -2.2%), an extremely fine step for a gross area scanning microscopic DIC investigation. Data recording for each

micro-DIC scan takes about an hour with the automated implementation of two correction measures that are conducted at each of the 450 (X, Y) frames to maintain the DIC quality [29]. The first is WD (and thereby focus) maintenance by taking Z-stacks of images and moving the sample to the Z position that has the best focus score. (This maintains WD within a fraction of the very limited DOF.) WD maintenance is absolutely mandatory for analyzable images with the utilized high-resolution optics. The second correction pertains to the maximum preservation of the material domain in each frame [minimizing material flow to and from neighboring frames in Fig. 3(b)] as deformation progresses. This is achieved by an FFT-based real-time DIC analysis of the frame with respect to its previous load image and moving the sample to rectify the calculated shift. Both procedures are automated in the custom instrument software coded in python. With the latter correction, there are no gaps in the (stitched) full-field strain maps when each frame is only analyzed with its counterpart in the reference domain.

DIC is conducted with the subset based inverse compositional algorithm [30] with first-order deformation mapping. 41×41-pixel subsets are used with 10-pixel (1 μm) grid spacing. Using rigid body motion tests (where the physical strain fields are null so that the DIC strains directly correspond to errors [31]), the DIC strain uncertainty is determined to be 0.2% for the utilized subset size and strain calculation procedure described in the next paragraph. The grid is overlaid on Fig. 3(d) to show the intragranular measurement resolution. Instrument code, DIC and data processing facilities utilize scientific python [32,33] and ImageJ [34,35] packages.

The displacement gradients $\partial u/\partial x, \partial u/\partial y, \partial v/\partial x, \partial v/\partial y$ are calculated from measured displacement fields (u, v) by using a 3×3 Savitzky-Golay differentiation kernel [36]. Local strains as high as 10% are generated in the measured fields closing on the application limit of small strain formulations. The difference with finite strain calculations is, however, still very limited and we will utilize the small strain and rotation tensor components for clarity of utilized notions:

$$\varepsilon_{xx} = \frac{\partial u}{\partial x}\ ,\ \varepsilon_{yy} = \frac{\partial v}{\partial y}\ ,\ \varepsilon_{xy} = \frac{1}{2}\left(\frac{\partial u}{\partial y} + \frac{\partial v}{\partial x}\right)\ ,\ \omega_{xy} = \frac{1}{2}\left(\frac{\partial u}{\partial y} - \frac{\partial v}{\partial x}\right) \qquad [1]$$

Strain ratio (apparent Poisson's ratio) over a selected field is defined as $\bar{\nu} = -\bar{\varepsilon}_{xx}/\bar{\varepsilon}_{yy}$ where overbar stands for field averaging. DIC among sequential loads are distinguished with "Δ", e.g., $\Delta\varepsilon_{yy}^{e-f}, \ldots, \Delta\omega_{xy}^{e-f}$ denote the results for load-point-*f* images analyzed with respect to load-point-*e* images.

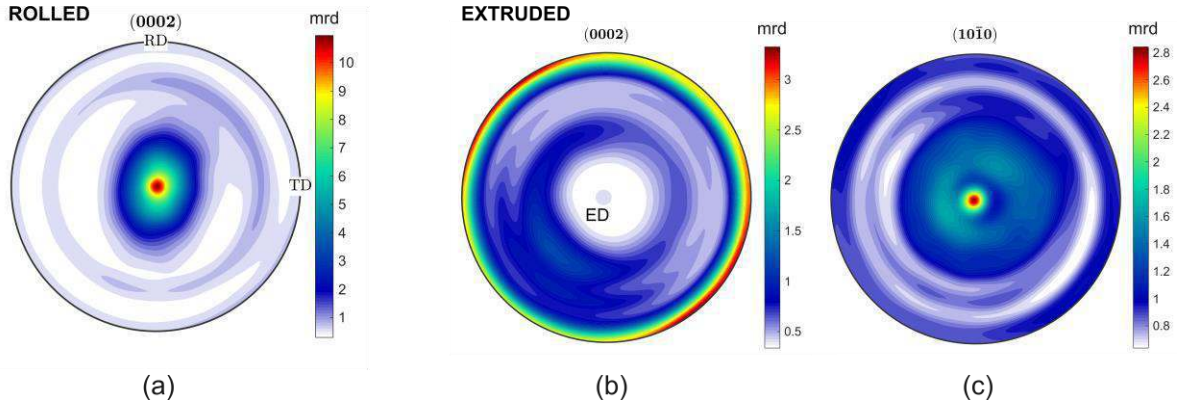

Figure 4. (a) (0002) pole figure for the rolled, and (b,c) (0002) and (10$\bar{1}$0) pole figures for the extruded Magnesium AZ31 materials used in the study. (mrd = multiples of random; RD, TD = rolled, transverse directions; ED=extrusion direction)

Finally, equivalent experimental and analysis procedures have been applied to another Mg AZ31 sample but with the *transversely isotropic* extrusion texture. This sample has the identical prismatic shape shown in Fig. 2, but EDM-cut from the central axis of a 22 mm diameter rod that is procured from Xi'an Yuechen with comparable grain size, determined to be 13 μm. This extruded sample is posed as a control experiment to reveal the nature of the strain/twinning fields due to this notch pattern *in the*

absence of severely anisotropic CTB formation. The crystallographic texture of both rolled and extruded materials considered in this study have been measured with x-ray diffraction. The data is collected with a Panalytical X-Pert Pro MPD four-circle diffractometer, and the orientation distribution functions are calculated with the MTEX [37] software. The c-axis (0002) pole figure of the rolled material generated by MTEX is shown in Fig. 4(a), presenting the preferential alignment of the c-axes with the ND direction. The (0002) pole figure of the extruded material [Fig. 4(b)], on the other hand, shows a preferred axisymmetric distribution of c-axes normal to the extrusion direction (ED). Thus, for the extrusion texture, crystallographic directions in the basal plane are concentrated about ED. This is demonstrated in Fig. 4(c) that shows the $(10\bar{1}0)$ pole figure.

RESULTS

The in situ micro-DIC fields that encompass approximately 1.5×10^5 grains sampled with ~1.5×10^7 data points at each load are presented in Fig. 5 with axial strain (ε_{yy}) contour maps. Due to space considerations, Fig. 5(a)-(k) considers 11 selected load points, a-k, that represent the salient features of the deformation stages while the ε_{yy} maps of all 30 micro-DIC points are provided in movie format as supplementary material. The engineering stress, σ, is plotted versus the axial strain averaged over the full micro-DIC field, $\bar{\varepsilon}_{yy}$, in Fig. 5(l)—absolute values are shown for viewing ease in this compression experiment. Over Fig. 5(l), points a-k and the remainder of the micro-DIC points are marked with filled and open circles, respectively. Strain fields of point i [Fig. 5(i)] are selected to be printed with a disproportionately large map in an attempt to better convey the resolution and micro-scale patterning of the fields in this deformation regime. (The aforementioned movie also offers improved resolution to better see the patterning in all the rest of the load points.) For comparison, the point-i *macro*-DIC map [Fig. 3(a,b)], which is naturally devoid of these details, is placed as an inset [Fig. 5(m)] over a dormant region of the corresponding micro-DIC map. The triangle symbols that mark the tips of the flat segments of each notch in Fig. 3(b) are carried over to Fig. 5(i) to unambiguously locate the notches over the strain maps. To save further space in the remaining maps of Fig. 5, only the flat segments between each triangle pair are marked (with red).

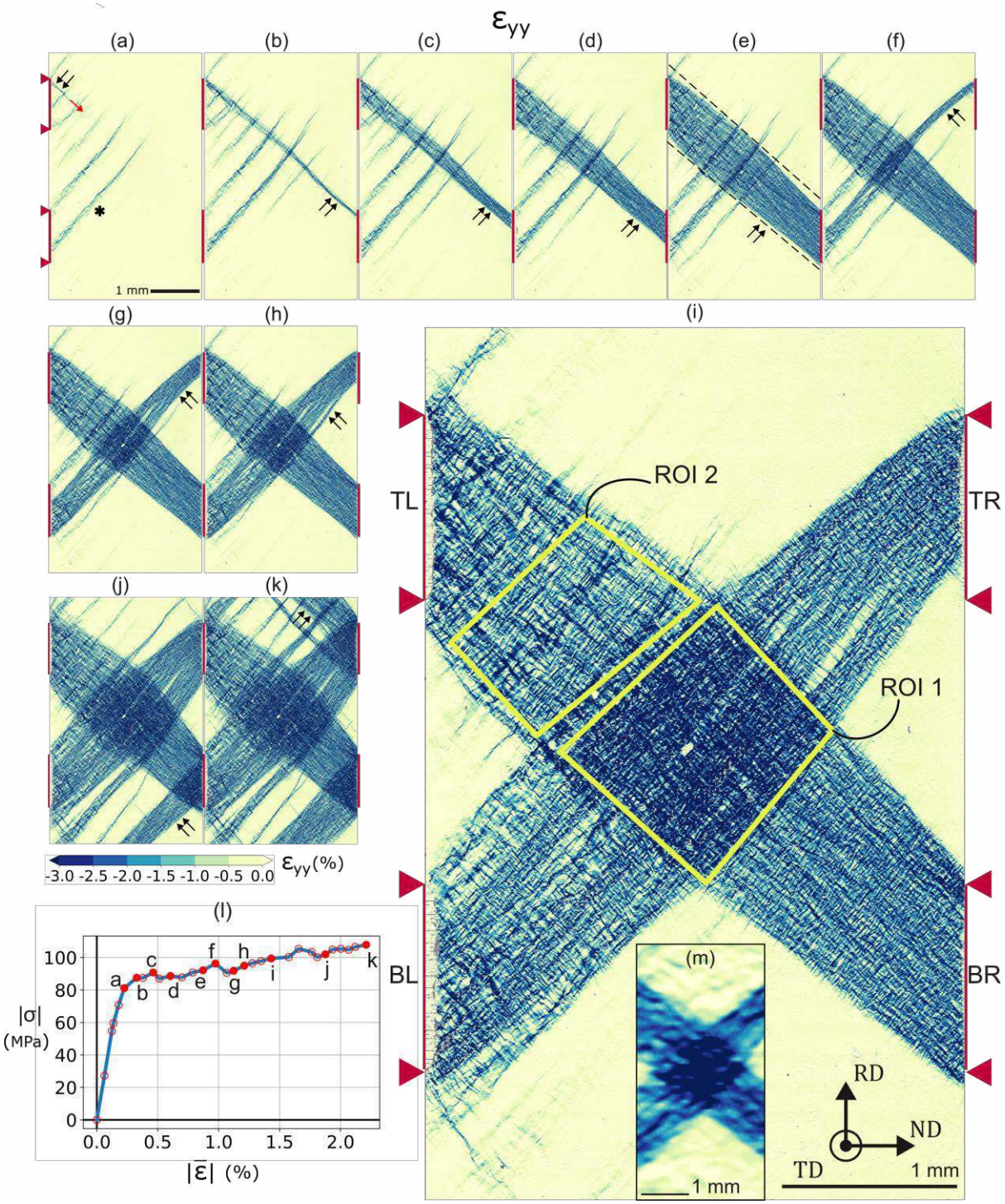

Figure 5. (a)-(k) Full-field (stitched) micro-DIC axial strain, ε_{yy}, maps at load points (a-k) indicated over (l), the engineering stress versus average strain curve of the sample under compression; (m) macro-DIC ε_{yy} map at point i for comparison.

At around the transition from the linear region to the twin plateau in the stress-strain curve [Fig. 5(l)], the strain localization (via coordinated twinning) starts with individual branches shooting out from notch corners as shown in Fig. 5(a). Out of these offshoots, the double (black) arrows next to the TL-notch in Fig. 5(a) mark a specific rudiment (i.e., a seed of collaborative twinning activity in a small grain cluster). There is a single (red) arrow next to this formation indicating the direction of its prospective advance. At the next load, this rudiment makes the first complete cross connection marked with double arrows in Fig. 5(b), fully extending from the TL notch to the BR notch. Next to the double

arrows, this formation is captured at only 50 µm (crudely 5 grains) thick, attesting to both the load/time-step and spatial resolution of the measurement. After point b, the strain accommodation proceeds by the lateral expansion of this -45° CTB [marked with double arrows over Fig. 5(c) to 5(e)], until the TL-BR corridor is roughly filled up. Then, consistent with the design goals of the sample, the activation of the opposite (+45°) BL-TR connection is observed. Two more intermediate points are provided in Fig. 5(g) and 5(h), showing the expansion of the BL-TR connection (marked with double arrows) to roughly fill up this notch corridor by point i [Fig. 5(i)]. One notes that the detailed morphology of this +45° crossing CTB family is influenced by the previously formed twinning structures, e.g., the initial +45° offshoot shown with an "*" in Fig. 5(a), leading to mild curving and a more interrupted lateral expansion. Aside from these necessarily sample-dependent details, one notes the primary outcome: the band formations have been guided to the designated corridors and the band intersection has been enforced at the predetermined location as targeted.

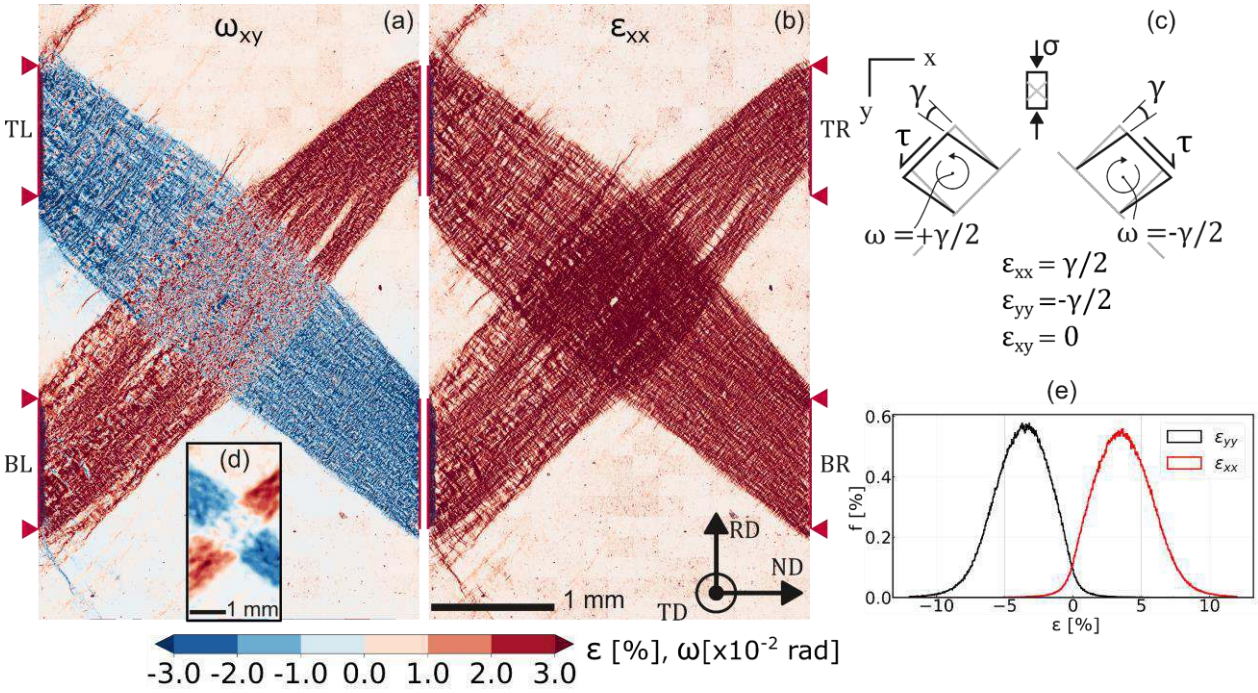

Figure 6. (a) Full field (stitched) micro-DIC small rotation (ω_{xy}), (b) transverse strain (ε_{xx}) maps at point i (see Fig. 5), (c) kinematic description of ideal +45° and -45° simple shear structures in the RD-ND (x-y) plane, (d) macro-DIC rotation (ω_{xy}) map for point i, (e) strain histogram for ε_{xx} and ε_{yy} sampled form region of interest 1 [see Figure 5(i)].

A more detailed quantitative analysis considers this point in time (i.e., point i). Two region of interests, ROI-1 at the central band overlap and ROI-2 outside the overlap (such that it exemplifies a zone of single-band activity) are defined on Fig. 5(i).Further, point-i in-plane infinitesimal rotation, ω_{xy}, and transverse strain, ε_{xx}, maps are complemented in Fig. 6(a) and 6(b), respectively. The effectively planar kinematics of the twinning bands allow a beneficial utilization of ω_{xy}, sketched in Fig. 6(c): The nominal +45° and -45° simple shear activity, while generating equivalent strains, lead to opposite sense rotations. Hence, with a colormap that emphasizes sense [red(+), blue(-) in this case], ω_{xy} maps automatically distinguish +45° and -45° simple shear structures. Accordingly, note the dominant blue [red] color of the -45° TL-BR [+45° BL-TR] band in the rotation maps in Fig. 6(a). When opposite sense shear structures superpose, the rotation will cancel out (while the strains add up). However, as an interesting side point, the realization of this cancellation is related to the measurement length-scale. The micro-DIC results resolve the micro-scale mesh of the macroscopic twinning bands while macro-DIC will find these bands to be largely monolithic [Fig. 5(m)] due to its larger effective averaging zone size. Similarly, macro-DIC rotation that is provided in Fig. 6(d) virtually cancels out in the overlap zone,

while micro-DIC fields of Fig. 6(a)—at the length-scale to capture discrete simple shear events in the overlap zone—predominantly shows a composition of +45° and -45° structures rather than a large-scale cancellation.

The final element of Fig. 6 is the histogram of ε_{xx} and ε_{yy} [Fig. 6(e)] that is sampled from ROI-1 for representing maximal strains in the field. It shows a near mirror symmetry (magnitude equality) of ε_{xx} and ε_{yy} distributions in conformance to the described planar shear kinematics. The implied extreme anisotropy of the formed bands can also be characterized by the effective strain ratio, $\bar{v}$, in Table I for two regions on interest marked on Fig. 5(i). $\bar{v}$ takes the value of 0.99 on the ROI-1 corresponding to the overlap of two bands and 0.95 on the ROI-2 chosen on the singular -45° band activity, both virtually consistent with the depiction in Fig. 1.

Table I. Axial and transverse strain averages and effective strain ratio values for rolled [point i, region of interests 1 and 2 shown in Fig. 5(i)] and extruded [point c, Fig. 7(c)] specimens.

	$\bar{\varepsilon}_{yy}$	$\bar{\varepsilon}_{xx}$	$\bar{v}$
Rolled, ROI 1	-3.7188	3.6818	0.99
Rolled, ROI 2	-2.2421	2.1222	0.95
Extruded, full field	-1.6093	0.8379	0.52

The average strains in the singular band ROI-2 are also provided in Table-1. Measuring from other singular band regions as well, region-averaged strain magnitudes are found to fall in 2.3±0.15%. This largely matches the literature values for the characteristic compactness of the singular twinning bands that formed over maiden fields in unnotched rolled samples of similar grain size (see Refs. [21,23]). This implies that the bands are guided rather than intensified with this (mild) notch design. When more strain is to be accommodated by the sample after both central corridors are filled (aside from some limited outward bulging of the TL-BR and BL-TR bands after point i), ±45° bands that are directed away from the gage center develop, shown with double arrows in Figs. 5(j) and 5(k).

The average strain in the overlap zone (ROI-1) has a magnitude of about 3.7% in Table I. While this value is significantly higher than the single band average strain, it is not doubling it either. Since the first band (TL-BR) goes over the maiden material, this suggests that the crossing band (BL-TR) imparts less strain at the overlap zone. Sequential DIC analysis (DIC with respect to the previous load point) results offer a much cleaner quantification of this proposition. To exemplify the trends and address the strains at the band intersection, Fig. 7 considers $\Delta\varepsilon_{yy}^{e-f}$. This strain increment between points e and f reveals the first +45° attack that has to cross over the filled-up TL-BR corridor. The dashes over Fig. 7(a) are carried over from Fig. 5(e) to show the approximate extent of the existing TL-BR band that has to be crossed. (Note the strict absence of further strain accommodation over the TL-BR band in the increment e-f.) Over the particular +45° strain-localization strip of Fig. 7(a), weaker fields in the overlap zone between the dashes are evident in comparison to the strains outside it that are accommodated over yet-undeformed material points. To quantify, the points of the +45° strip are first selected with a combination of high strain thresholding and a binary closing operation [23]. The resultant mask is shown in Fig. 7(c). Fig. 7(b) plots columnar average (along y-axis with a column thickness of Δx=5 μm with Gaussian smoothing) of $\Delta\varepsilon_{yy}$ for the selected points as a function of horizontal position. The band strain matches the characteristic singular band strain level outside the overlap (about 2.4%) while it shows a clear 20-25% drop to the 1.85% level at the overlap. This is a direct measurement of the dilution of the strain activity of a coordinated twining band as it crosses the band of the opposite family.

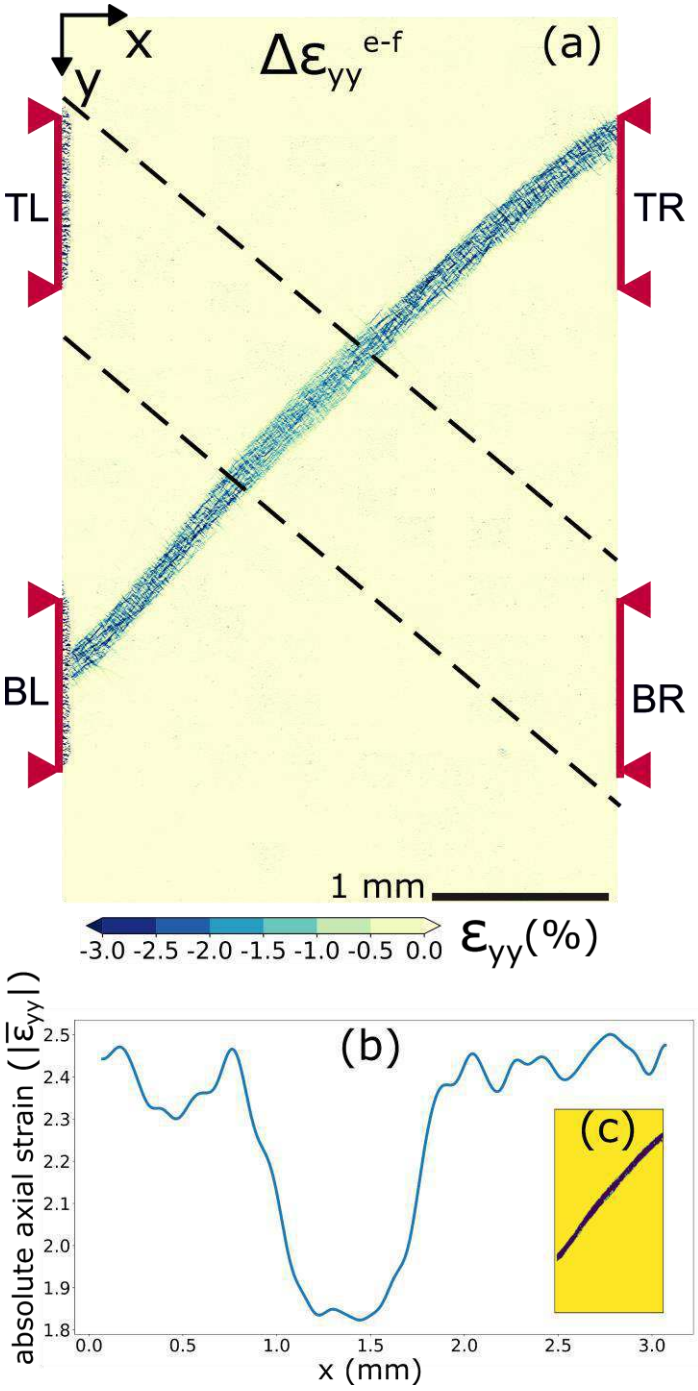

Figure 7. (a) Sequential micro-DIC axial strain ($\Delta\varepsilon_{yy}^{e-f}$) map, showing results for the DIC analysis of point-f image array with respect to point-e image array; the dashes indicate the location of the opposite sense macroscopic band that the current band formation has to cross through [see Fig. 5(e)], (b) column average of axial strain over only the band points shown with dark color in part (c). This mask is formed by strain thresholding and binary closing operations.

As a general note over Fig. 7, note the $\Delta\varepsilon_{yy}$ fields are practically null outside the current CTB attack—not at all typical for the strain accommodation of a generic metallic polycrystal. This point can also be noted over all $\Delta\varepsilon_{yy}$ maps, again provided in movie format as supplementary material, showing the strictness of the Lüders-type strain accommodation. One will benefit from watching the $\Delta\varepsilon_{yy}$ movie in conjunction with the absolute strain ε_{yy} movie, observing the standalone incremental realization of the

discussed kinematic processes (e.g., lateral expansion of the band over points b-e, outward bulging of the crossing bands after point i, dilution across intersections with existing CTBs, etc.)

In this study, the cross-notch pattern, with notches specifically carved along TD, has been employed to guide extremely anisotropic and abrupt shear bands whose plane of shear coincides with the RD-ND plane. To further put the uniqueness of this application in perspective, Fig. 8(a-c) shows ε_{yy} maps for a control experiment where *extruded* Mg AZ31 is given the same notch pattern and compressed along the extrusion direction (ED). In this load path, the deformation again entails profuse twinning. The texture for extruded Magnesium [Fig. 4(b,c)] is an axisymmetric distribution of c-axes about ED, however, and the material shows transverse isotropy when loaded along ED.Note, the top (observation) and side surfaces of this prismatic sample geometry (Fig. 2) are random transverse planes. The effective stress-strain curve and the location of the points a-c are provided in Fig. 8(d).

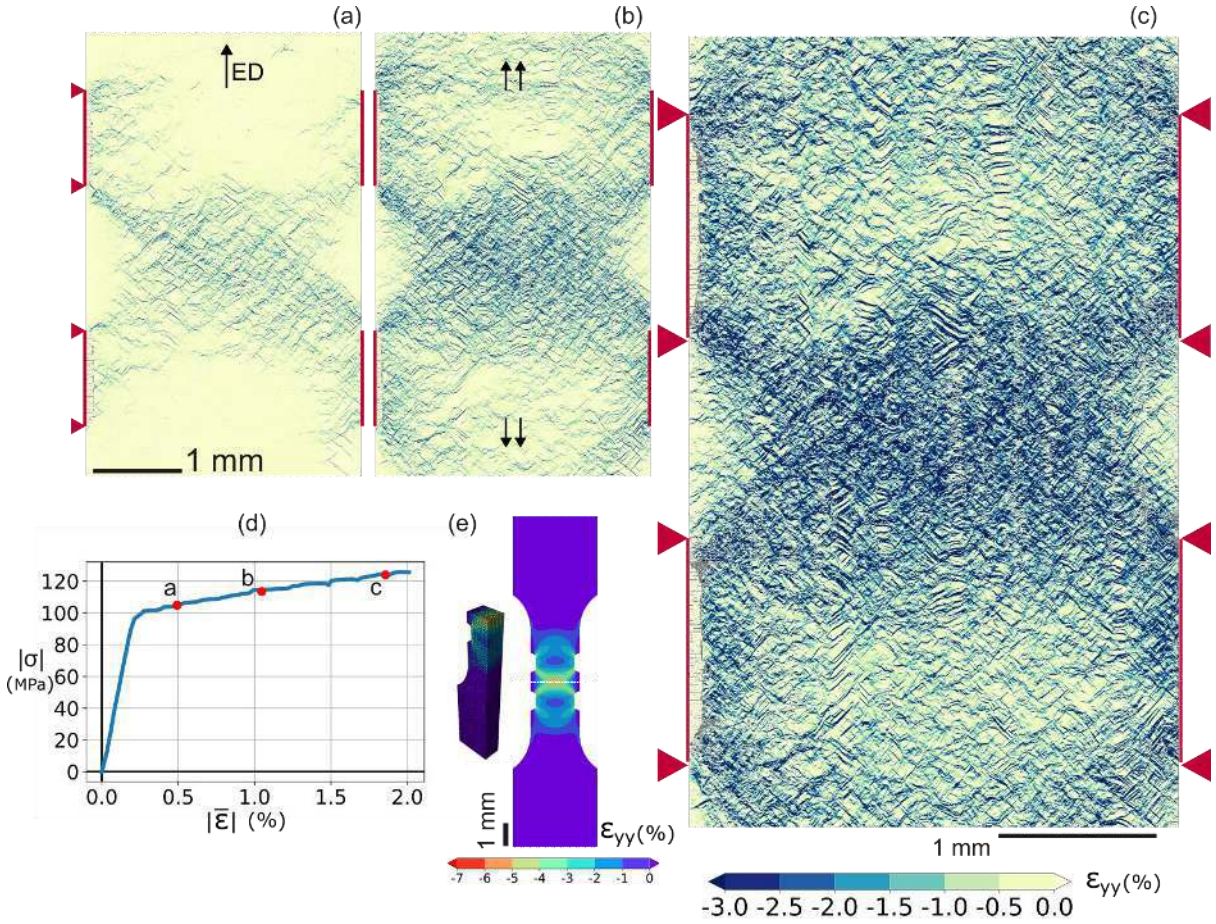

Figure 8. (a) - (c) Axial strain maps, (d) engineering stress-axial macro strain curve of the transversely isotropic extruded sample under compression, (e) axial strain contours (at 1.5% absolute average strain) on the surface of a 3D finite element analysis (actual analysis domain on the left) that considers isotropic Mises plasticity.

Even at the very beginning of the twin plateau [Fig. 8(a)], the twin patterns immediately form loosely, covering extensivespace in the gage section without any clear band formation and advance. While the activity is most concentrated at the sample center, strain structures that originate at the notches but are directed away from the gage center, also form. Such formations are connected by point-b [double arrows in Fig. 8(b)], creating a localization pattern that is crudely in the shape of the number "8". Point-c patterns [Fig. 8(c)] show a spread of the twin activity to the full gage area but with preferential intensification of the 8-shaped high strain zones. To contrast with the extreme $\bar{\nu}$ values of the rolled sample deformation structures, the full-field effective strain ratio of this extruded sample is added to Table 1. The listed value (0.52) is virtually equivalent to the isotropic value (0.5) for isochoric

deformation processes. As shown in Fig. 8(e), the 8-shaped localization with maximal intensity at the gage center also agrees with a simple isotropic Mises plasticity finite element analysis of this sample geometry. This is a 3-D analysis [symmetric domain shown in Fig. 8(e)] that is input the flow curve of Fig. 8(d) and conducted in ABAQUS™ software.

More clearly, the FE analysis represents the localization patterns that would form in this unusual sample geometry for a routine isotropic elastic-plastic aggregate. The *macro-scale* strain distribution that is realized in a transversely isotropic (extruded) Magnesium alloy aggregate is found to largely conform to this pattern though it still deforms by profuse twinning.(Note the micro-scale patterning due to twinning is evident in Fig. 8(a-c).) This contrasts the strain accommodation in the rolled sample (Figs. 5-7) for which this sample geometry has been designed for†.

Finally, we note that samples with only one offset-notch-pair (i.e., only retain the TL-BR pair in Fig. 2, removing the BL-TR pair) have also been successfully tested in the laboratory to guide a single family of bands that are first initialized in the field. One more cross-notched sample is also tested, reproducing identical salient features observed in this experiment.

DISCUSSION

Mechanical twinning is a sudden event when a band of material inside a crystallite abruptly switches (acoustic emission [38], high-speed DIC over single crystal Mg [39]) to a new orientation, instantly bringing about a large transformation strain (principal strain magnitude ~6.5% for the observed Magnesium tensile twin) in the process. If this process spatially coordinates ("twin transmission"), an autocatalytic advance of twinning runs across the crystal, causing Lüders-like band formation. As a meso-scale (intergranular) phenomenon that *governs* the material response to load, the length-scale band (μm-mm) of DIC with area-scanning optical microscopy has been particularly suited to elaborate this event. Previously, Aydıner and Telemez (2014) [22] and Shafaghi et al. (2020) [23] utilized an in situ version of this method with multiple load points over the twin plateau. The former used enlarged grains (through annealing) to achieve intragranular resolution but was able to present the extreme kinematics (recall Fig. 1) of this phenomenon for rolled Magnesium AZ31 under RD-compression for the first time. Here, "extreme" pertains to the material being a polycrystalline aggregate; the authors are not aware of another polycrystalline aggregate (Lüders banding or not) that virtually deforms with an extruded two-dimensional deformation pattern (Fig. 1). They also reported that the band formations/advances are abrupt, analogous to their root micro-mechanism. Shafaghi et al. [23] used high-NA optics at 20x magnification over the as-received grain size (in the same 10 μm order as in this study). By improving post-processing to select band regions directly, Shafaghi et al. quantifies the characteristic mean CTB strains (analogous to Lüders strain [40]) to be around 2.3%. Another laboratory (Anten and Scholtes, 2019) provided confirmation, reporting 2.5% with macroscopic DIC over similar microstructure [21]. The quantitative band measurements in Shafaghi et al. [23] also lead to the computation of the extreme $\bar{\nu} \cong 1$ over the bands. The interaction of CTBs have not been investigated so far, however, which is carried out in the current implementation over the enforced CTB crossing. Notably, the primary result (Fig. 7) is obtained via switching to a sequential DIC analysis that allows a direct quantitative assessment. The band attack that proceeded through the previously formed CTB is found to be diluted by 20-25% at the overlap, presumably due to the hardening imposed on this region by the first band. In this *quantitative* study of the overlap zone, the role of the notches is to engineer this overlap at the center of the measurement domain.

† To avoid a misunderstanding, let us state that the cross-notched sample geometry is not appropriate if the aim is to regulate the twinning activity in extruded samples per se. (The extruded sample study here is a perspective point.) A single pair of aligned notches is the obvious choice for concentrating/guiding twinning fields (e.g., as in [42]) in ED-compressed extruded samples.

In Fig. 5, the seed formation, advance and expansion stages of the CTBs are presented with unique detail thanks to a much higher time-step resolution over Refs. [22,23]. The functional role of the notches is again to ascertain the location of the CTB seed formations—in previous work, seeds commonly form outside the measurement box, e.g., closer to the transition between the gage and the grip section [23]. Recall the CTB advances are abrupt and microscopic DIC simply reveals the intermediate equilibrium states. The minimum thickness of a sudden band formation (under quasi-static strain rates of all these studies) was another question that could not be addressed previously. With the super fine time-stepping in this study, band formations that are few-to-several grains thick are presented over Fig. 5(b) and many more can be noted in the $\Delta\varepsilon_{yy}$ video. The current study also offers roughly doubled spatial resolution with respect to its predecessors [22,23], yielding a four-fold increase in data points per grain. Thus, the resolution of the current data set is significantly better than what has been contributed to literature so far, and this reflects in the much larger data sizes per load (15×10^6 here vs. 3×10^6 in Shafaghi et al. [23]).

Guiding the bands in an overlapping pattern has clearly been envisioned when this sample has been designed, though the dilution of the crossing band or the quantitative degree of this dilution could not be known (but had to be measured). One other fact that could not be guessed a priori is that the CTB compactness remains the same as those in unnotched samples (same average strains of ~2.3%). If anything, the lack of intensification inside the offset-notch channels might be found unintuitive [since the nominal shear stress is higher in the offset-notch corridors with less area in the lateral section that connects TL-BR (or BL-TR) notches] but can perhaps be reasoned with the already high compactness of the CTBs. Once CTBs form with their characteristic compactness in a stratified fashion [Fig. 5(a-i)], no further eruption is favored inside these hardened fields despite the higher stress. CTBs instead are driven outwards toward the maiden material fields.

In terms of the target length-scale, high-fidelity polycrystalline modeling efforts are in rough agreement with the presented micro-DIC data set . They can, hence, presumably benefit from the statistical/spatial aspects of the presented results. In this field, spatially resolved models that intend to capture local fields on realistic grain neighborhoods [14–17] have been gaining increasingly more ground. This approach is eyeing toward predicting material damage and failure [16]. There is an additional motivation for Magnesium alloys that led to intense effort on crystal plasticity approaches for this material in last three decades. If universal crystal plasticity models can be conceived for Magnesium, they can predict the plethora of different behavior this material exhibits for various crystallographic textures and load paths (e.g., [41]). The CTB deformation regime that is detailed with qualitative (e.g., crude thickness of CTB events) and quantitative measures here (e.g., the mean strain content of CTB advance as it crosses another band or maiden fields) puts extremely hard targets for current models. The models will naturally assume differing degrees of homogenization in time and over space to function, but these efforts should not refrain from looking at exactly how the material behaves and aspire to meet it at varying levels. (Otherwise, the goal of local fidelity and damage prediction becomes defunct.) Meeting mean strains in CTB advances might be a sensible first target. If the model is universal, it will predict the extrusion texture fields (e.g., localities in Fig. 8) just as well upon the mere change of input crystallographic texture.

While this is by and large a scientific effort conducted over the de facto standard magnesium alloy in scientific efforts (AZ31), AZ-series is the most standard wrought Magnesium class in engineering as well. Simply, the samples of this study are extracted from commonly available wrought metals. The Magnesium practitioner is familiar with the fact that the deformation behavior of the Magnesium alloys assumes vastly different regimes (micro-mechanism combinations) depending on the crystallographic texture and load path. The spatial aspect of this dependence seems to be not nearly as well known, though it has been shown that the twin proliferation leads to very different strain accommodation patterns in rolled and extruded samples [24]. Given this difference among unnotched samples, the

disparity shown in this study on how the twinning fields interact with geometric disturbances in rolled and extruded samples (Fig. 5 vs. Fig. 8) is largely comprehensible.

Since intense strain localization is typically undesirable from an engineering perspective, it is important to point out the exact material subset where the sharp shear-banding fields of Fig. 5 will be realized. While we consider an RD-compressed sample with notches carved along TD (with notch planes normal to ND), the crucial microstructural elements remain essentially the same for any in-plane sample so long as the notches are carved with their planes normal to ND. As can be seen from the (0002) pole figure of this plate as well [Fig. 4(a)], the texture shows approximate symmetry about ND and the mechanical response of in-plane samples show very little variation [5]. As such, TD, RD, and intermediate in-plane loading directions are commonly regarded under the same umbrella of in-plane compression and tension (IPC and IPT) samples (see, e.g., [4]). In this vein, any IPC sample with the notch planes normal to ND is expected to behave as in Fig. 5 since the fundamental microstructural element (c-axes//ND) remains identical. Other than that, this regime will not be realized in wrought Magnesium with classical textures. In detail, it will not materialize in any case where the load direction does not favor the unipolar twinning (e.g., IPT samples) and any case that favors twinning but with transverse isotropy about the loading axis [e.g., compression along ED (utilized as a counterexample in Fig. 8) or tension along ND in rolling texture.]

Plates are the most common form of wrought metals for extracting components and these components are typically cut out from the (RD-TD) plane of the plate. Since they can be put under compression, IPC-type loading can be pretty common for these alloys. Further, the engineering components can contain notch-like features for weight reduction or connections. This paper hence can offer an awareness to the Magnesium practitioner on how twin-related shear band structures might develop in components under IPC-type loading, or it can perhaps provide a general explanation to some observed patterns.

Aside from an awareness perspective, we can note that an array of notches on either side of the sample, can create a cross-mesh of CTB bands with overstrained overlap zones (similar to the overlap zone of this sample but multiple intersections at desired locations). The authors simply do not know if this truss-like deformation patterning can be useful but postulate it as a curious possibility.

We can make more clear statements for a middle point between science and engineering, namely, experimentation that further investigates the twin transmission behavior over CTBs in IPC samples. The need to geometrically constrain the collaborative twinning behavior for technical reasons is apparent in, e.g., a future high-speed imaging study that investigates the speed of twin transmission. In these very fast experiments, it is important to allocate the pixels of the camera carefully, and prefixing the event location is critical. Such studies can employ this proven notch pattern.

CONCLUSIONS

Based on the previously explored kinematics of the severely anisotropic coordinated twinning bands in rolled Magnesium, a cross-notched sample design is proposed to regulate the activity of these bands, guiding them across vertically offset notch pairs. The progression of the deformation in this sample has been in situ examined by a unique microscopic DIC implementation with its composition of spatial resolution, spatial coverage, and time-step resolution.

The initial coordinated twinning structures that form are offshoots from notch corners. When one of these rudiments makes an across-the-sample connection among an offset notch pair, the mode of strain accommodation switches to the lateral expansion of the coordinated twinning band. This continues until the offset notch pair corridor is filled up. The strain average of the bands is on par with the values from unnotched samples in literature. Hence, the bands are guided rather than concentrated with this sample design.

This process is realized sequentially for both offset notch pairs, and the band formation across the second is enforced to go across the first over the predetermined overlap region. Hence, a controlled study of the band interactions has been made possible. Through sequential DIC analysis, we find that the band proceeds with its typical compactness outside the overlap but with a reduced strain content (by 20-25%) through it.

A transversely isotropic polycrystalline aggregate of the same material (extruded Mg AZ31) is used as a control experiment. Its twin proliferation fields contrast the Lüders banding with strict geometry that was controlled in the rolled sample.

As with any material, rolled plates are the most common form of raw material (that is fed to machining operations) for wrought Magnesium alloys adding to the technological importance of this study. Predetermining the band fronts can also be crucial in scientific experimentation, e.g., in studies that explore the material behavior with extreme temporal resolution where the number of pixels and data collection duration have strict limits. Finally, the polycrystal models that attempt micro-scale fidelity for twinning Magnesium require quantitative and controlled studies of coordinated twin activity such as this one. Though very hard targets, both the standalone and band-crossing CTB compactness should be matched by microscopically “correct” models of Magnesium.

ACKNOWLEDGEMENTS

This work was supported by the Scientific and Technological Research Council of Turkey (TÜBİTAK), Grant No: 120N722. LS also acknowledges mobility funding from Campus France (Programme Bosphore – No 46626ZM).

APPENDIX A. SUPPLEMENTARY DATA

Two files in movie format are provided:

1) absoluteaxialstrain_microDIC_movie.mp4: A file that contains axial strain maps of all load points in loading order. The average strain and point number is added to the top right corner of the movie.

2) incrementalaxialstrain_sequentialmicroDIC_movie.mp4: A file that contains incremental strain maps that stem from DIC between sequential data points. The point numbers are shown on the top right corner, e.g., [1]-[2] is the incremental strain field among points [1] and [2].

DATA AVAILABILITY

Data will be made available upon request.

REFERENCES

[1] J.W.W. Christian, S. Mahajan, Deformation twinning, Prog Mater Sci. 39 (1995) 1–157. https://doi.org/10.1016/0079-6425(94)00007-7.

[2] J. Zhang, S.P. Joshi, Phenomenological crystal plasticity modeling and detailed micromechanical investigations of pure magnesium, J Mech Phys Solids. 60 (2012) 945–972. https://doi.org/10.1016/j.jmps.2012.01.005.

[3] A.L. Oppedal, H. el Kadiri, C.N. Tomé, G.C. Kaschner, S.C. Vogel, J.C. Baird, M.F. Horstemeyer, Effect of dislocation transmutation on modeling hardening mechanisms by twinning in magnesium, Int J Plast. 30–31 (2012) 41–61. https://doi.org/10.1016/j.ijplas.2011.09.002.

[4] S.R. Agnew, C.N. Tomé, D.W. Brown, T.M. Holden, S.C. Vogel, Study of slip mechanisms in a magnesium alloy by neutron diffraction and modeling, Scr Mater. 48 (2003) 1003–1008. https://doi.org/10.1016/S1359-6462(02)00591-2.

[5] X.Y. Lou, M. Li, R.K. Boger, S.R. Agnew, R.H. Wagoner, Hardening evolution of AZ31B Mg sheet, Int J Plast. 23 (2007) 44–86. https://doi.org/10.1016/j.ijplas.2006.03.005.

[6] K. Hazeli, H. Askari, J. Cuadra, F. Streller, R.W. Carpick, H.M. Zbib, A. Kontsos, Microstructure-sensitive investigation of magnesium alloy fatigue, Int J Plast. 68 (2015) 55–76. https://doi.org/10.1016/j.ijplas.2014.10.010.

[7] S. Kleiner, P.J. Uggowitzer, Mechanical anisotropy of extruded Mg–6% Al–1% Zn alloy, Materials Science and Engineering: A. 379 (2004) 258–263. https://doi.org/10.1016/j.msea.2004.02.020.

[8] S.M. Yin, H.J. Yang, S.X. Li, S.D. Wu, F. Yang, Cyclic deformation behavior of as-extruded Mg–3%Al–1%Zn, Scr Mater. 58 (2008) 751–754. https://doi.org/10.1016/j.scriptamat.2007.12.020.

[9] L. Wu, S.R. Agnew, Y. Ren, D.W. Brown, B. Clausen, G.M. Stoica, H.R. Wenk, P.K. Liaw, The effects of texture and extension twinning on the low-cycle fatigue behavior of a rolled magnesium alloy, AZ31B, Materials Science and Engineering A. 527 (2010) 7057–7067. https://doi.org/10.1016/j.msea.2010.07.047.

[10] H. Qiao, S.R. Agnew, P.D. Wu, Modeling twinning and detwinning behavior of Mg alloy ZK60A during monotonic and cyclic loading, Int J Plast. 65 (2015) 61–84. https://doi.org/10.1016/j.ijplas.2014.08.010.

[11] H. Abdolvand, M.R. Daymond, Multi-scale modeling and experimental study of twin inception and propagation in hexagonal close-packed materials using a crystal plasticity finite element approach; part II: Local behavior, J Mech Phys Solids. 61 (2013) 803–818. https://doi.org/10.1016/j.jmps.2012.10.017.

[12] O. Muránsky, M.R. Barnett, V. Luzin, S. Vogel, On the correlation between deformation twinning and Lüders-like deformation in an extruded Mg alloy: In situ neutron diffraction and EPSC.4 modelling, Materials Science and Engineering: A. 527 (2010) 1383–1394. https://doi.org/10.1016/j.msea.2009.10.018.

[13] M. Arul Kumar, I.J. Beyerlein, R.A. Lebensohn, C.N. Tomé, Modeling the effect of neighboring grains on twin growth in HCP polycrystals, Model Simul Mat Sci Eng. 25 (2017). https://doi.org/10.1088/1361-651X/aa7bbb.

[14] A. Vidyasagar, A.D. Tutcuoglu, D.M. Kochmann, Deformation patterning in finite-strain crystal plasticity by spectral homogenization with application to magnesium, Comput Methods Appl Mech Eng. 335 (2018) 584–609. https://doi.org/10.1016/j.cma.2018.03.003.

[15] J. Cheng, S. Ghosh, Crystal plasticity finite element modeling of discrete twin evolution in polycrystalline magnesium, J Mech Phys Solids. 99 (2017) 512–538. https://doi.org/10.1016/j.jmps.2016.12.008.

[16] J. Cheng, J. Shen, R.K. Mishra, S. Ghosh, Discrete twin evolution in Mg alloys using a novel crystal plasticity finite element model, Acta Mater. 149 (2018) 142–153. https://doi.org/10.1016/j.actamat.2018.02.032.

[17] C. Mareau, M.R. Daymond, Micromechanical modelling of twinning in polycrystalline materials: Application to magnesium, Int J Plast. 85 (2016) 156–171. https://doi.org/10.1016/j.ijplas.2016.07.007.

[18] A. Githens, S. Ganesan, Z. Chen, J. Allison, V. Sundararaghavan, S. Daly, Characterizing microscale deformation mechanisms and macroscopic tensile properties of a high strength magnesium rare-earth alloy: A combined experimental and crystal plasticity approach, Acta Mater. 186 (2020) 77–94. https://doi.org/10.1016/j.actamat.2019.12.012.

[19] C. Mo, A. Kontsos, Twinning contributions to strain localizations in magnesium alloys, Materials Science and Engineering A. 722 (2018) 206–215. https://doi.org/10.1016/j.msea.2018.03.024.

[20] K. Hazeli, J. Cuadra, P.A.A. Vanniamparambil, A. Kontsos, In situ identification of twin-related bands near yielding in a magnesium alloy, Scr Mater. 68 (2013) 83–86. https://doi.org/10.1016/j.scriptamat.2012.09.009.

[21] K. Anten, B. Scholtes, Formation of macroscopic twin bands and inhomogeneous deformation during cyclic tension-compression loading of the Mg-wrought alloy AZ31, Materials Science and Engineering A. 746 (2019) 217–228. https://doi.org/10.1016/j.msea.2019.01.033.

[22] C.C. Aydıner, M.A. Telemez, Multiscale deformation heterogeneity in twinning magnesium investigated with in situ image correlation, Int J Plast. 56 (2014) 203–218. https://doi.org/10.1016/j.ijplas.2013.12.001.

[23] N. Shafaghi, E. Kapan, C.C. Aydıner, Cyclic Strain Heterogeneity and Damage Formation in Rolled Magnesium Via In Situ Microscopic Image Correlation, Exp Mech. 60 (2020) 735–751. https://doi.org/10.1007/s11340-020-00612-6.

[24] E. Kapan, N. Shafaghi, S. Uçar, C.C. Aydıner, Texture-dependent character of strain heterogeneity in Magnesium AZ31 under reversed loading, Materials Science and Engineering A. 684 (2017) 706–711. https://doi.org/10.1016/j.msea.2016.12.085.

[25] Y.R. Paudel, J. Indeck, K. Hazeli, M.W. Priddy, K. Inal, H. Rhee, C.D. Barrett, W.R. Whittington, K.R. Limmer, H. el Kadiri, Characterization and modeling of $\{10\bar{1}2\}$ twin banding in magnesium, Acta Mater. 183 (2020) 438–451. https://doi.org/10.1016/j.actamat.2019.11.020.

[26] M.R. Barnett, M.D. Nave, A. Ghaderi, Yield point elongation due to twinning in a magnesium alloy, Acta Mater. 60 (2012) 1433–1443. https://doi.org/10.1016/j.actamat.2011.11.022.

[27] I.J.J. Beyerlein, L. Capolungo, P.E.E. Marshall, R.J.J. McCabe, C.N. Tome, C.N. Tomé, Statistical analyses of deformation twinning in magnesium, Philosophical Magazine. 90 (2010) 2161–2190. https://doi.org/10.1080/14786431003630835.

[28] İ.B. Üçel, E. Kapan, O. Türkoğlu, C.C. Aydıner, In situ investigation of strain heterogeneity and microstructural shear bands in rolled Magnesium AZ31, Int J Plast. 118 (2019) 233–251. https://doi.org/10.1016/j.ijplas.2019.02.008.

[29] N.A. Özdür, I.B. Üçel, J. Yang, C.C. Aydıner, Residual Intensity as a Morphological Identifier of Twinning Fields in Microscopic Image Correlation, Exp Mech. 61 (2021) 499–514. https://doi.org/10.1007/s11340-020-00672-8.

[30] B. Pan, K. Li, W. Tong, Fast, Robust and Accurate Digital Image Correlation Calculation Without Redundant Computations, Exp Mech. 53 (2013) 1277–1289. https://doi.org/10.1007/s11340-013-9717-6.

[31] H. Haddadi, S. Belhabib, Use of rigid-body motion for the investigation and estimation of the measurement errors related to digital image correlation technique, Opt Lasers Eng. 46 (2008) 185–196. https://doi.org/10.1016/j.optlaseng.2007.05.008.

[32] P. Virtanen, R. Gommers, T.E. Oliphant, M. Haberland, T. Reddy, D. Cournapeau, E. Burovski, P. Peterson, W. Weckesser, J. Bright, S.J. van der Walt, M. Brett, J. Wilson, K.J. Millman, N. Mayorov, A.R.J.J. Nelson, E. Jones, R. Kern, E. Larson, C.J. Carey, İ. Polat, Y. Feng, E.W. Moore, J. VanderPlas, D. Laxalde, J. Perktold, R. Cimrman, I. Henriksen, E.A. Quintero, C.R. Harris, A.M. Archibald, A.H. Ribeiro, F. Pedregosa, P. van Mulbregt, SciPy 1.0 Contributors, A. Vijaykumar, A. pietro Bardelli, A. Rothberg, A. Hilboll, A. Kloeckner, A. Scopatz, A. Lee, A. Rokem, C.N. Woods, C. Fulton, C. Masson, C. Häggström, C. Fitzgerald, D.A. Nicholson, D.R. Hagen, D. v. Pasechnik, E. Olivetti, E. Martin, E. Wieser, F. Silva, F. Lenders, F. Wilhelm, G. Young, G.A. Price, G.L. Ingold, G.E. Allen, G.R. Lee, H. Audren, I. Probst, J.P. Dietrich, J. Silterra, J.T. Webber, J. Slavič, J. Nothman, J. Buchner, J. Kulick, J.L. Schönberger, J.V. de Miranda Cardoso, J. Reimer, J. Harrington, J.L.C. Rodríguez, J. Nunez-Iglesias, J. Kuczynski, K. Tritz, M. Thoma, M. Newville, M. Kümmerer, M. Bolingbroke, M. Tartre, M. Pak, N.J. Smith, N. Nowaczyk, N. Shebanov, O. Pavlyk, P.A. Brodtkorb, P. Lee, R.T. McGibbon, R. Feldbauer, S. Lewis, S. Tygier, S. Sievert, S. Vigna, S. Peterson, S. More, T. Pudlik, T. Oshima, T.J. Pingel, T.P. Robitaille, T. Spura, T.R. Jones, T. Cera, T. Leslie, T. Zito, T. Krauss, U. Upadhyay, Y.O. Halchenko, Y. Vázquez-Baeza, SciPy 1.0: fundamental algorithms for scientific computing in Python, Nat Methods. 17 (2020) 261–272. https://doi.org/10.1038/s41592-019-0686-2.

[33] S. van der Walt, J.L. Schönberger, J. Nunez-Iglesias, F. Boulogne, J.D. Warner, N. Yager, E. Gouillart, T. Yu, Scikit-image: Image processing in python, PeerJ. 2014 (2014) 1–18. https://doi.org/10.7717/peerj.453.

[34] C.T. Rueden, J. Schindelin, M.C. Hiner, B.E. DeZonia, A.E. Walter, E.T. Arena, K.W. Eliceiri, ImageJ2: ImageJ for the next generation of scientific image data, BMC Bioinformatics. 18 (2017) 529. https://doi.org/10.1186/s12859-017-1934-z.

[35] S. Preibisch, S. Saalfeld, P. Tomancak, Globally optimal stitching of tiled 3D microscopic image acquisitions, Bioinformatics. 25 (2009) 1463–1465. https://doi.org/10.1093/bioinformatics/btp184.

[36] B. Pan, Full-field strain measurement using a two-dimensional Savitzky-Golay digital differentiator in digital image correlation, Optical Engineering. 46 (2007) 033601. https://doi.org/10.1117/1.2714926.

[37] F. Bachmann, R. Hielscher, H. Schaeben, Texture Analysis with MTEX – Free and Open Source Software Toolbox, Solid State Phenomena. 160 (2010) 63–68. https://doi.org/10.4028/www.scientific.net/SSP.160.63.

[38] D. Drozdenko, J. Bohlen, S. Yi, P. Minárik, F. Chmelík, P. Dobroň, Investigating a twinning–detwinning process in wrought Mg alloys by the acoustic emission technique, Acta Mater. 110 (2016) 103–113. https://doi.org/10.1016/j.actamat.2016.03.013.

[39] V. Kannan, K. Hazeli, K.T. Ramesh, The mechanics of dynamic twinning in single crystal magnesium, J Mech Phys Solids. 120 (2018) 154–178. https://doi.org/10.1016/j.jmps.2018.03.010.

[40] W.M. Lomer, The yield phenomenon in polycrystalline mild steel, J Mech Phys Solids. 1 (1952) 64–73. https://doi.org/10.1016/0022-5096(52)90007-0.